Volume 21
Number 36
28 September 2025
Pages 6997–7176

Soft Matter

rsc.li/soft-matter-journal

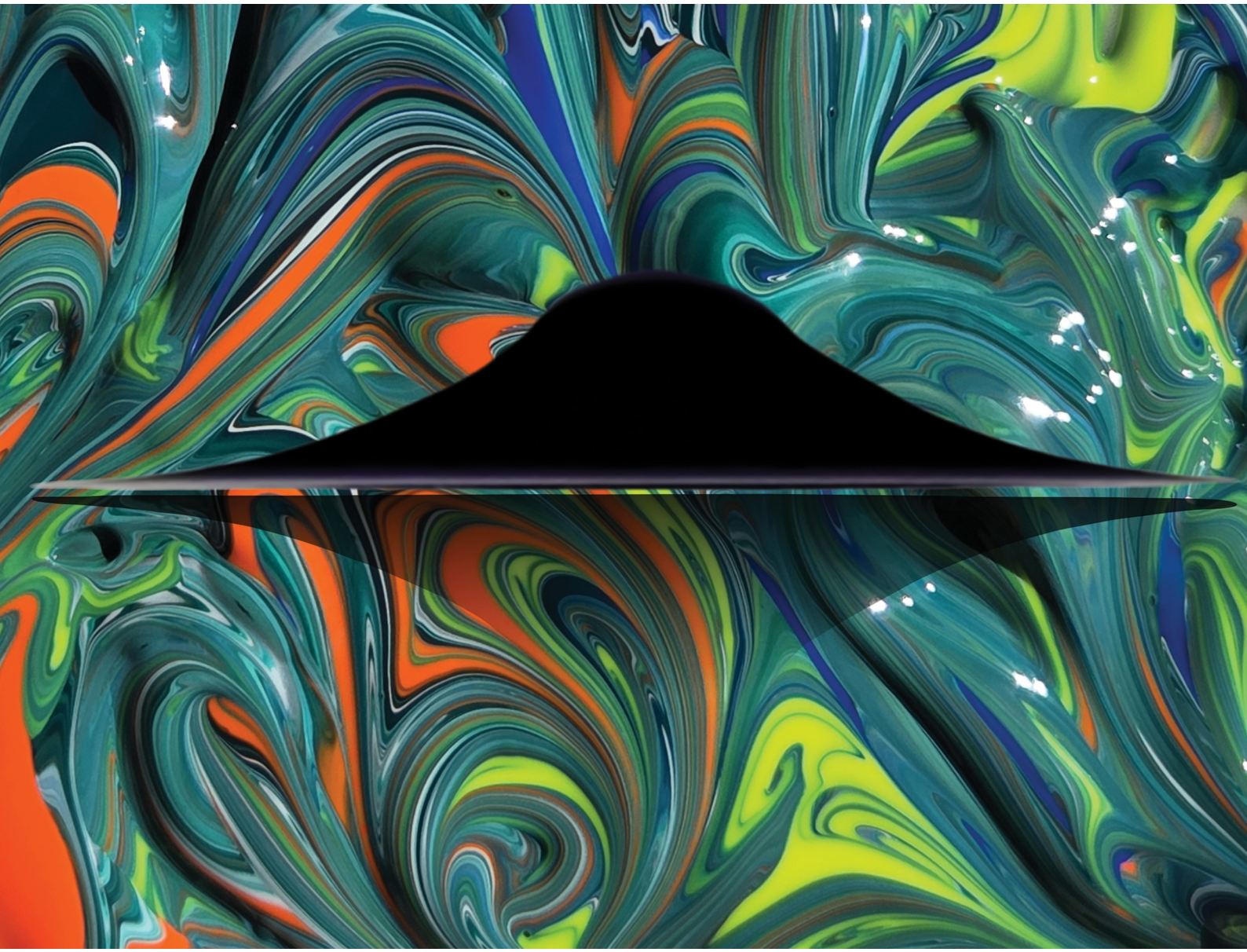

ISSN 1744-6848

ROYAL SOCIETY OF CHEMISTRY

COMMUNICATION
Marcel Moura *et al.*
Droplet spreading in a wedge: a route to fluid rheology for power-law liquids

20 YEARS ANNIVERSARY

Soft Matter

COMMUNICATION

View Article Online
View Journal | View Issue

Check for updates

Cite this: *Soft Matter*, 2025, **21**, 7014

Received 18th March 2025,
Accepted 5th July 2025

DOI: 10.1039/d5sm00286a

rsc.li/soft-matter-journal

Open Access Article. Published on 07 ervence 2025. Downloaded on 04.02.2026 12:14:37.
This article is licensed under a Creative Commons Attribution 3.0 Unported Licence.

Droplet spreading in a wedge: a route to fluid rheology for power-law liquids†

Marcel Moura, [a] Vanessa Kern, [b] Knut Jørgen Måløy, [ac] Andreas Carlson [bd] and Eirik G. Flekkøy *[ae]

Measuring the rheology of liquids typically requires precise control over shear rates and stresses. Here, we describe an alternative route for predicting the characteristic features of a power-law fluid by simply observing the capillary spreading dynamics of viscous droplets in a wedge-shaped geometry. In this confined setting, capillary and viscous forces interact to produce a spreading dynamics described by anomalous diffusion, a process where the front position grows as a power-law in time with an exponent that differs from the value 1/2 found in classical diffusion. We derive a nonlinear diffusion equation that captures this behavior, and we show that the diffusion exponent is directly related to the rheological exponent of the fluid. We verify this relationship by using both experiments and simulations for different power-law fluids. As the predictions are independent from flow-specific details, this approach provides a robust tool for inferring rheological properties from the spreading dynamics.

The spreading of droplets on solid surfaces is a ubiquitous phenomenon, observable in everyday events such as raindrops falling on a window, as well as in a variety of biological, geological, and physical systems. In these contexts, it can serve as a mechanism for delivering nutrients to living cells,[1] oxidating substances to minerals,[2] or forming fluid pathways within complex geometries.[3,4] The spontaneous spreading of fluids depends on the wetting properties and geometry of the medium through which it spreads.[5–9] However, it also depends crucially on the rheology of the liquid, as is well known from the everyday application of non-Newtonian fluids, such as toothpaste, corn starch, paint, yogurt and shampoo. Controlling fluid rheology is also topical in industrial applications and in food science,[10–17] where it covers everything from cooking recipes to consumer satisfaction.[18] In this study, we show that the spreading dynamics of a droplet of a power-law liquid can be used to predict the fluid's rheological properties.

The rheology of a power-law fluid is characterized by the fact that the shear stress is given by a power of the strain rate. The spreading of such a liquid in a wedge-shaped geometry is anomalous in the sense that it is described in the same way as anomalous diffusion. Mathematically, it is captured by a non-linear diffusion equation that yields analytical solutions with a spreading rate which is given by an anomalous diffusion exponent.[19–22] As an interesting by-product, we obtain a relationship between the exponent governing the rheology and the diffusion exponent. As this relationship depends only on the conservation of fluid mass and a non-linear Darcy law, which relates the volume flux to the pressure gradient, it is independent of other details of the flow structure. The rheological exponent may thus be obtained solely on the basis of the spontaneous (capillary driven) fluid motion, without any type of force- or shear-rate control, as needed in commercial rheometers.

The analysis and findings presented here complement the extensive literature on anomalous diffusion. Pattle[23] noted, already in 1959, that the seepage of a liquid into a cloth or porous body could be described by a nonlinear diffusion equation, yielding sub-diffusive spreading of the fluid. In the 1980s, there was a large effort to understand the nature of anomalous diffusion, particularly in the context of transport in disordered and porous media. In porous media flows, strong confinement often gives rise to regimes where transport occurs through corners and thin films. In these cases, the balance between capillary and viscous forces plays a key role and can enable persistent, long-range transport[5,24–27] such as when connecting otherwise disconnected fluid clusters.[28–36] Our solution, which pertains to a viscous flow driven by capillarity as a droplet spreads in an idealized (sharp) wedge, see Fig. 1a, with a constant solid–liquid contact angle, may thus serve as a baseline model for more complex flow geometries.

[a] *PoreLab, The Njord Center, Department of Physics, University of Oslo, NO-0316 Oslo, Norway. E-mail: flekkoy@fys.uio.no*
[b] *Department of Mathematics, University of Oslo, NO-0316 Oslo, Norway*
[c] *PoreLab, Department of Geoscience and Petroleum, Norwegian University of Science and Technology, NO-7031 Trondheim, Norway*
[d] *Department of Medical Biochemistry and Biophysics, Umeå University, Umeå, Sweden*
[e] *PoreLab, Department of Chemistry, Norwegian University of Science and Technology, NO-7491 Trondheim, Norway*

† Electronic supplementary information (ESI) available. See DOI: https://doi.org/10.1039/d5sm00286a

This journal is © The Royal Society of Chemistry 2025

Open Access Article. Published on 07 ervence 2025. Downloaded on 04.02.2026 12:14:37.
This article is licensed under a Creative Commons Attribution 3.0 Unported Licence.

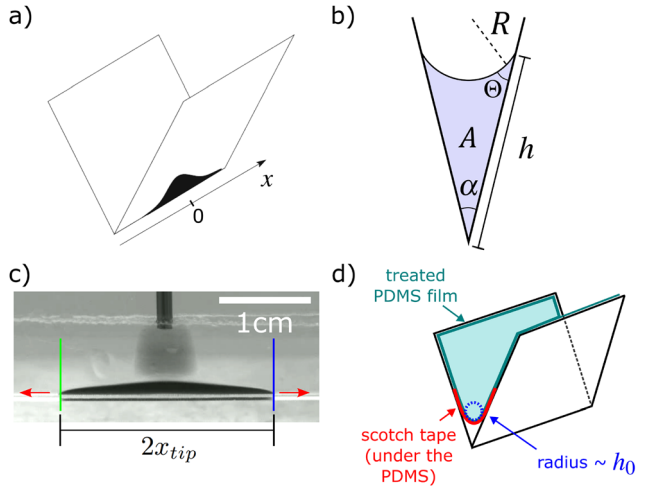

Fig. 1 (a) Liquid droplet spreading in a wedge. (b) The cross-sectional area A and the local height h of the spreading droplet, which both vary along the wedge. Here, $\alpha = 30^\circ$ is the opening angle of the wedge, and Θ is the contact angle at the liquid–solid–air contact line. (c) Snapshot of the experiment, where the green and blue vertical lines denote the left and right tip position, and the red arrows indicate the spreading direction. (d) Diagram illustrating the Scotch tape (red) and PDMS layer (cyan) employed, which lead to an effective finite radius of curvature h_0 in the corner (exaggerated in the figure for clarity). Note that the main difference between the idealized (sharp) wedge and the experimental setup is a finite curvature where the plates meet.

A key finding in our study is the fact that the position of the tip of a droplet spreading in a wedge geometry scales with time as $x_{tip} \propto t^{\tau}$, where the exponent τ is directly linked to the rheological exponent n characterizing the power-law fluid. By contrast, when the spreading of a shear-thinning fluid happens in radial fashion on a plane,[37,38] rather than along a corner line, the exponent governing the spreading rate has been shown to depend very weakly on the rheological exponent.[38] Our theoretical prediction and measurements of the Newtonian spreading exponent $\tau \approx 0.4$ are consistent with the value $\tau \approx 1/3$ that has been measured for Newtonian flow of different liquids that imbibe along a corner from an infinite reservoir.[39,40] This suggests that the hydrodynamics is strongly governed by the dynamics at the tip and less sensitive to the boundary condition where the fluid is supplied.

A droplet of a power-law fluid spreading in a wedge is characterized by the stress–strain relationship $\sigma \propto \dot{\gamma}^n$ over a certain range of the strain rate $\dot{\gamma}$, which is frequently described by the Ostwald–de Waele model.[13] The viscosity is then given by

$$\mu = \eta_0 \dot{\gamma}^{n-1} = \mu_0 \left(\frac{\dot{\gamma}}{\dot{\gamma}_0}\right)^{n-1}, \quad (1)$$

where μ_0 and μ are in units of Pa s, the exponent $n = 1$ corresponds to a Newtonian fluid, and $\dot{\gamma}_0$ is a reference strain rate at which the liquid is non-Newtonian. We shall take $\dot{\gamma}_0 = 10\ s^{-1}$ for the fluids employed in this study (see the rheological characterization of the fluids in the ESI†). Many polymer melts and solutions exhibit a value of n in the range 0.3–0.7, depending upon the concentration and molecular weight of the polymer.[41,42] Even smaller values of the power-law exponent (n = 0.1–0.15) are encountered with fine particle suspensions like kaolin-in-water, bentonite-in-water, *etc.* By using polyacrylamide solutions of different concentrations, Ansari *et al.*[43] measured a range of power-law indices n = 0.26–0.47, which were obtained for shear rates in the range 10–1000 s^{-1}. See also Jouenne and Levache[44] for a comprehensive dataset on the rheology of acrylamide-based polymer solutions.

We shall obtain a prediction for the height $h(x, t)$ of a droplet of a power-law fluid when spreading along the wedge geometry, as shown in Fig. 1. Our power-law liquid wets the surface inside the wedge and spreads due to the capillary forces, as illustrated in Fig. 1a. Its shape is described by the height $h(x, t)$. When the wetting angle $\Theta < (\pi - \alpha)/2$, α being the opening angle of the wedge (see Fig. 1b), the capillary pressure will be negative, and the minimal energy will be reached when the solid–liquid contact area is maximized. This occurs when the liquid spreads out as far as possible along the wedge. The negative capillary pressure drives the flow and increases in magnitude towards the tips of the drop as $1/h$, since the radius of curvature of the liquid–air interface $R \propto h$, see Fig. 1b. In Fig. 1c we show a snapshot of the experiment, where the red arrows denote the spreading direction. It is worth noting that in the experimental setup, the wedge is not perfectly sharp as in the idealized model. Instead, a small radius of curvature h_0 exists along the bottom edge, see Fig. 1d. This curvature arises from the procedure employed to build the setup, which involves coating the glass slides that form the wedge walls with a PDMS film. Further details are provided in the ESI.†

In the ESI,† we show that the volumetric flow rate q across a surface normal to the corner line may be written

$$q = Q_n \left(\frac{-\partial P/\partial x}{\eta_0}\right)^{1/n} h^{3+1/n}, \quad (2)$$

where P is the capillary pressure, x is the coordinate along the wedge, $h(x)$ is the height of the liquid in the normal direction, and

$$Q_n = \frac{2^{\frac{1+n}{2n}} n^2}{(2n+1)(3n+1)} \left(\frac{\alpha}{2}\right)^{\frac{1+n}{2n}} \quad (3)$$

is a dimensionless average of the flow field, which is dependent on our choice of flow geometry, but not its length scale. See also Guyon *et al.*[45] for further details on lubrication flows and complex fluids.

In order to obtain an analytical solution, our theoretical approach ignores: (1) the effects of gravity and inertia, (2) the finite initial droplet width and the interface curvature in the x-direction, (3) the cut-offs in shear rates where the non-Newtonian behavior becomes Newtonian, (4) the finite curvature of the corner geometry, and (5) dynamic variation of the contact angle Θ and pinning effects.

Approximating the contact angle by $\Theta = 20^\circ$, the curvature of the liquid interface $1/R$ sets the capillary pressure difference across this interface to be

$$P(x) = -\frac{\cos(\Theta + \alpha/2)\sigma}{h(x)\sin(\alpha/2)}, \quad (4)$$

Open Access Article. Published on 07 ervence 2025. Downloaded on 04.02.2026 12:14:37.
This article is licensed under a Creative Commons Attribution 3.0 Unported Licence.

where σ is the liquid–air surface tension and we have applied a simple geometric argument to replace R by h and the relevant angles shown in Fig. 1b.

The relative magnitude of gravitational to capillary forces is estimated as the ratio between the hydrostatic pressure drop $\rho g h$ and the capillary pressure drop given in eqn (4). Ignoring the cosine term in this expression yields the ratio

$$\frac{\rho g h^2}{\sigma}\sin(\alpha/2) \approx 0.15 \tag{5}$$

for all the experiments. The fraction is well below unity, justifying the neglect of gravity in the theory. Here we have set h = 2 mm, which is a typical maximum value during the observation time of the experiments, and the opening angle of the wedge is $\alpha = 30^\circ$. The fluid density ρ and surface tension σ do not differ significantly from pure water.

In order to estimate the relative importance of inertial forces, we calculate the Reynolds number for each experiment, that is, the ratio of the steady inertial and viscous terms of the Navier–Stokes equation. The quantity u_m represents a characteristic mean tip velocity, measured as the ratio x_{tip}/t in the late-time regime of the experiment, where the scaling $x_{tip} \propto t^\tau$ holds. While the actual velocity decreases over time, u_m serves as a useful reference for the typical velocity observed during the experiment. Calculating a relevant Reynolds number requires some care, as the viscous term $\propto \nabla^2 u$ is dominated by the shear forces from the wall and thus governed by the width of the droplet, while the inertial term $\propto \mathbf{u}\cdot\nabla\mathbf{u}$ is governed by variations along the flow and hence the droplet half-width x_{tip}. As a result we define the relevant Reynolds number as

$$\mathrm{Re} = \frac{u_m L_{eff}}{\nu^*} \tag{6}$$

with the effective length $L_{eff} = (\alpha h/2)^2/x_{tip} \approx 10^{-5}$ m when the typical value for the droplet half-width is $x_{tip} \approx 2$ cm. Here, ν^* is the kinematic viscosity which we shall extract from Fig. S1 (ESI†) as the value in the Newtonian regime. In Table 1 the values of Re for the different experiments are given, showing that inertia is indeed negligible, and more so for the higher XG-concentrations.

Assuming the fluids to be in the non-Newtonian regime is clearly not correct everywhere. Since the shear rate will be close to zero at $x = 0$, there will always be regions of slow Newtonian flow. However, since the capillary forces and viscous dissipation take on their maximum values at $x = \pm x_{tip}$, the spreading process is likely to be strongly dominated by the hydrodynamics right at the droplet tips. For that reason, we compare the shear rate there to the critical crossover shear rate $\dot\gamma_c$, where the rheology becomes Newtonian. Taking h_0 to be the only relevant length scale for the flow at the tips, we estimate the tip shear rate as $\dot\gamma_{tip} = u_m/(\alpha h_0/2)$. Table 1 shows the typical shear rate, $\dot\gamma_{tip}$, and how it compares with the crossover shear rates $\dot\gamma_c$ obtained from Fig. S1 (ESI†). Note that in all cases $\dot\gamma_{tip} > \dot\gamma_c$, although only by a small margin for the largest concentrations. We will include the influence of a finite corner curvature in our numerical solutions by setting the volumetric flow rate to $q = 0$ when h falls below a threshold h_0, see Fig. 1d.

Table 1 Characteristic values of the flow velocity u_m, shear rate at the droplet tips $\dot\gamma_{tip}$, and Reynolds number Re. The threshold shear rate $\dot\gamma_c$, at which non-Newtonian behavior sets in, is shown in parentheses alongside $\dot\gamma_{tip}$. The values of $\dot\gamma_c$ are obtained from Fig. S1 (ESI), which also provides the corresponding kinematic viscosity values $\nu^* = \eta/\rho$. The Reynolds number is calculated as $\mathrm{Re} = u_m L_{eff}/\nu^*$, where the effective length $L_{eff} \approx 10^{-5}$ m

XG [g L^{-1}]	u_m [m s^{-1}]	ν^* [m^2 s^{-1}]	$\dot\gamma_{tip}$ ($\dot\gamma_c$) [s^{-1}]	Re
0	1×10^{-2}	5×10^{-6}	70 (0)	2×10^{-2}
0.5	1×10^{-2}	1×10^{-5}	70 (3)	1×10^{-2}
1	6×10^{-3}	4×10^{-5}	40 (2)	1×10^{-3}
2	1×10^{-3}	2×10^{-4}	7 (0.8)	5×10^{-5}
3	5×10^{-5}	2×10^{-3}	0.35 (0.2)	1×10^{-7}
4	4×10^{-5}	4×10^{-3}	0.3 (0.1)	1×10^{-7}
6	2×10^{-5}	2×10^{-2}	0.15 (0.08)	1×10^{-8}

It is the variations in $h(x)$ that will cause a pressure gradient along the wedge, and we may invoke eqn (2) to get the mean flow. The cross-sectional area in the direction normal to x, $A(x) \approx (\alpha/2)h^2$, and the amount of liquid volume is a conserved quantity, so that

$$\frac{\partial A}{\partial t} + \frac{\partial q}{\partial x} = 0\,. \tag{7}$$

Expressing h by A in eqn (2) and using eqn (4), the volume conservation may then be written on the form

$$\frac{\partial A}{\partial t} = -D_0\frac{\partial}{\partial x}\left(A^{3/2-1/n}\left(-\frac{\partial A}{\partial x}\right)^{1/n}\right), \tag{8}$$

where the 'diffusion coefficient'

$$D_0 = \left(\frac{2}{\alpha}\right)^{3/2}\left(\frac{\sigma}{\eta_0}\frac{\cos(\Theta+\alpha/2)}{2\sin(\alpha/2)}\right)^{1/n} Q_n \tag{9}$$

has dimensions of m$^{1/n}$ s^{-1}.

Since the solution $A(x, t)$ is symmetric around $x = 0$, we will only consider $x > 0$, so that $\partial P/\partial x < 0$. By taking the initial condition to be $A(x, 0) = V_0\delta(x)$, where V_0 is the droplet volume, we shall follow[20] and seek a scaling solution of the form

$$A(x, t) = \frac{p(u)}{f(t)}, \tag{10}$$

where

$$u = \frac{x}{f(t)}. \tag{11}$$

This solution has the property that $\int \mathrm{d}x A(x, t) = \int \mathrm{d}u p(u) = V_0$. In order to insert eqn (10) in eqn (8), we need the derivative, $\partial A/\partial t = (f'(t)/f(t)^2)\mathrm{d}(up)/\mathrm{d}u$, which allows us to write eqn (8) in the form

$$\frac{f'(t)}{D_0 f^{-1/2-1/n}} = \frac{\left(p^{3/2-1/n}(-\mathrm{d}p/\mathrm{d}u)^{1/n}\right)'}{-\mathrm{d}(up)/\mathrm{d}u} = \lambda\,, \tag{12}$$

This journal is © The Royal Society of Chemistry 2025

Open Access Article. Published on 07 ervence 2025. Downloaded on 04.02.2026 12:14:37.
This article is licensed under a Creative Commons Attribution 3.0 Unported Licence.

where we have separated the u and t-dependent terms with the separation constant λ. Integration of the $f(t)$-part of eqn (12) is straightforward and yields

$$f(t) = \left(\frac{\lambda D_0 t}{\tau}\right)^{\tau}, \tag{13}$$

with

$$\tau = \frac{2n}{2+3n}. \tag{14}$$

The p-part of eqn (12) takes the form, $((\mathrm{d}/\mathrm{d}u)(p^{3/2-1/n}\cdot(-\mathrm{d}p/\mathrm{d}u)^{1/n}) - \lambda up) = 0$, which may be integrated to give $p^{3/2-1/n}(-p'(u))^{1/n} - \lambda up = K$. Since, by symmetry, $p'(0) = 0$ and $p(0)$ must be finite, the integration constant $K = 0$, and the above equation may be rearranged to give $p^{n/2-1}p' = \lambda^n u^n$. This may be integrated to give

$$p(u) = \lambda^2\left(\frac{n}{2(n+1)}\right)^{2/n}\left(L^{n+1} - u^{n+1}\right)^{2/n}, \tag{15}$$

where the normalization condition yields the integration constant $L = \lambda^{-\tau}(V_0/A_n)^{\tau/2}$ with $A_n = 2(n/(2(n+1)))^{2/n}\int_0^1 \mathrm{d}y\left(1-y^{n+1}\right)^{2/n}$. Inserting this L-value in $A(x,t) = p(u)/f(t)$, λ cancels out, and so we are free to choose $\lambda = \dot{\gamma}_0/D_0$ in order to make

$$f(t) = \left(\frac{\dot{\gamma}_0 t}{\tau}\right)^{\tau} \tag{16}$$

dimensionless. Then, $L(D_0) = ((D_0/\dot{\gamma}_0)(V_0/A_n)^{1/2})^{\tau}$, where the dimension of u is m and that of $p(u)$ is m^2. Inserting λ in eqn (15) finally yields

$$p(u) = \left(\frac{\dot{\gamma}_0}{D_0}\right)^2\left(\frac{n}{2(n+1)}\right)^{2/n}\left(L^{n+1}(D_0) - u^{n+1}\right)^{2/n}. \tag{17}$$

Requiring that $p(u)$ be real restricts this solution to the x-domain where $L^{n+1} - u^{n+1} > 0$, or $|u| < L$. Outside

$$x_{\mathrm{tip}}(t) = Lf(t) = \left(\left(\frac{V_0}{A_n}\right)^{1/2}\frac{D_0 t}{\tau}\right)^{\tau}, \tag{18}$$

$A(x,t)$ then vanishes exactly, so that $2x_{\mathrm{tip}}(t)$ is the extent of the droplet.

The fact that $x_{\mathrm{tip}} \propto t^{\tau}$ is a key result as it provides the link between the spreading rate and the diffusion exponent τ, and by eqn (14), the rheological exponent n. The $\tau = 0.4$ value for $n = 1$ agrees with the result found by Hansen *et al.*,[21] who solved eqn (8) in the special case of a Newtonian liquid. The τ-exponent is simply obtained by plotting the experimental $x_{\mathrm{tip}}(t)$-values on a log–log plot. Having obtained the τ and n-values from $x_{\mathrm{tip}}(t)$ in this way, the scaling function $f(t)$ is known and may be used to obtain a data collapse for the experimental values of $A(x,t)f(t)$ *versus* $x/f(t)$ as predicted by theory. With this experimental data collapse, fitting eqn (17) to the data using D_0 as a fitting parameter gives D_0. The rheological prefactor μ_0 may then in principle be obtained by solving eqn (9) with respect to $\mu_0 = \eta_0\dot{\gamma}_0^{n-1}$ as

$$\mu_0 = \left(\frac{2}{\alpha}\right)^{3n/2}\frac{\sigma\cos(\Theta+\alpha/2)}{2\sin(\alpha/2)}\left(\frac{Q_n}{D_0}\right)^n\dot{\gamma}_0^{n-1}, \tag{19}$$

provided a constant contact angle. However, as is well known, the static contact angle, which we measure to be $\Theta \approx 20^{\circ}$, will in general be replaced by a dynamic contact angle Θ_{dyn} once the contact line is moving. Hoffmann[46] showed that the difference between Θ_{dyn} and Θ is governed by the local capillary number Ca *via* a general scaling relation. Later, Sheng[47] and Kokko-Latva and Rothmann[48] showed that this relation is well approximated by $\cos(\Theta) - \cos(\Theta_{\mathrm{dyn}}) \propto \mathrm{Ca}$ with a prefactor of order unity. The capillary number Ca is the ratio of viscous to capillary forces, so in our case $\mathrm{Ca} \sim 1$, since these are the dominating forces that govern the flow, in particular close to x_{tip}.

Also, since the analytic theory ignores the corner curvature h_0, an experimentally measured value of $h(x,t)$ (the distance from the curved corner to the meniscus) will be associated with an overestimated value of the capillary pressure that drives the flow. This will predict a faster overall spreading rate than what is actually observed. This effect thus has the opposite influence of the dynamic contact angle increasing above the static one, which will lead to a slower spreading. For these reasons μ_0 cannot be obtained from eqn (19) unless Θ_{dyn} is measured independently and used instead of Θ, and the corner is made sufficiently sharp.

The mathematical model can be solved numerically, and the solutions provide testable predictions. To test these predictions, we design an experimental system consisting of two thin transparent plates, arranged at an angle $\alpha = 30^{\circ}$ and securely held by a support mechanism (see Fig. 1). Standard microscope glass slides (dimensions 76 mm × 26 mm × 1 mm) were used. One critical experimental aspect was to ensure a high level of wettability with the wedge and minimize impurities that may affect the contact-line motion. As such, the plates were coated with a thin polymeric layer of PDMS, modified with a hydrophilic agent (methyl-terminated poly(dimethylsiloxane-*b*-ethylene oxide)). The coating was further treated with nitrogen plasma to enhance the wettability.[49] We tested a range of different fluids, including mixtures of xanthan gum (XG)[50] and water at varying concentrations, as well as a glycerol–water mixture to represent the Newtonian case. The XG concentration in water was systematically varied from 0.5 g L^{-1} to 6 g L^{-1}. For further details about the coating procedure and fluids preparation, see the ESI.†

In the experiment the wedge's corner is not infinitely sharp, rather it has a radius of curvature $h_0 \approx 0.6$ mm due to the finite thickness of the PDMS coating, see Fig. 1d. To mimic the experiments, we solve eqn (7) numerically, introducing a Gaussian initial profile for $h(x,t)$ and a cut-off corresponding to the corner curvature. This cut-off arises because the capillary pressure changes sign approximately at the point where $h(x,t)$ becomes smaller than h_0, see Fig. 1d. We set the radius of curvature $h_0 = 0.6$ mm and the initial profile half-width

Open Access Article. Published on 07 ervence 2025. Downloaded on 04.02.2026 12:14:37.
This article is licensed under a Creative Commons Attribution 3.0 Unported Licence.

w_0 = 0.8 mm throughout in the numerical calculations, similar to the experiments. This may be represented mathematically by imposing $q = 0$ in eqn (7), where $h(x, t) < h_0$. Eqn (8) can then be integrated numerically using centered spatial derivatives and an explicit first-order time stepping scheme.

Fig. 2a shows the temporal evolution of the droplet spread x_{tip}, measured as half of the distance between the left and right tips of the droplet, marked in Fig. 1b, for seven experiments going from the Newtonian case (leftmost curve) to the most shear-thinning case (rightmost curve). Arbitrary horizontal shifts have been applied to the curves for better visualization. The linear range in the x_{tip} plot allows the determination of τ by use of eqn (18). Fig. 2b shows a comparison between the measured τ-values against their theoretical predictions. The experimentally and numerically measured exponents are denoted τ_{exp} and τ_c, and the theoretical values τ_{th} are computed from eqn (14). The errorbars shown are due to the uncertainty in the fitting of the data from Fig. 2b. We notice that the experimental data tends to gather under the one-to-one τ_{th}-line. We attribute this divergence to the fact that in the experimental setup we do not have a sharp wedge. However, the numerically estimated exponents for which this finite curvature radius h_0 is taken into account, agree with the experimental measurements from Fig. 2b within the error bar in these data, except for the smallest and largest τ-values.

At the largest τ-value (the Newtonian case) the discrepancy is still moderate and may be linked to the difference in the Newtonian and non-Newtonian behavior near the contact line. On the other hand, the discrepancy at the smallest τ-value is likely caused by a departure from the non-Newtonian domain of the power-law fluid, which happens at sufficiently small shear rates. In the ESI,† we show how the numerical τ-values depend on h_0 and converges to the analytical result as $h_0 \to 0$. Variations of the initial half-width w_0 in the 0–2 mm range has less than a 1% effect on the τ-values as initial Gaussian profiles converge quickly to the profiles of eqn (17) (see ESI†).

Fig. 3a shows the experimental profiles $h(x, t)$ for the spreading of a drop at a XG-concentration of 2 g L^{-1} and V_0 = 19 mm^3, while Fig. 3b shows the data collapse implied by eqn (10) and (11) outside the domain where the corner curvature introduces a cut-off. The numerical results capture this behavior, while also showing a close agreement between the analytic and numerical results in the central region. Note that the collapse also verifies the scaling $x_{tip} \propto t^{\tau}$ while the agreement between the analytic and numerical results implies a very fast relaxation towards the analytical prediction.

For the experimental determination of the cross-sectional area $A(x, t)$ employed in Fig. 3b, a correction due to the

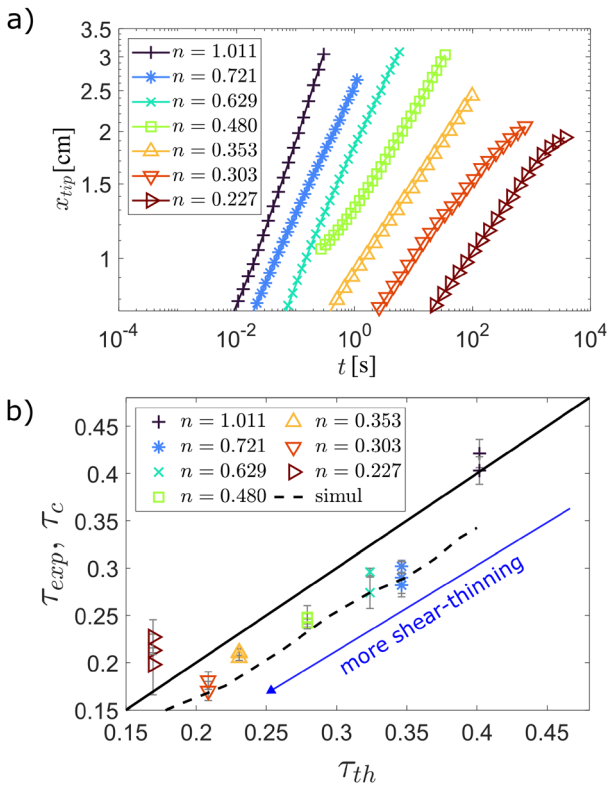

Fig. 2 (a) Experimentally measured droplet spread $x_{tip}(t)$. The curves are shifted horizontally by arbitrary values to aid visualization. The leftmost curve corresponds to the Newtonian fluid, while the others are from XG fluids with XG concentrations of 0.5, 1, 2, 3, 4 and 6 g L^{-1} increasing from left to right. (b) Comparison between the experimental exponent τ_{exp} (symbols) and numerical exponent τ_c (dashed line), as well as the theoretical slopes τ_{th} computed from eqn (14) (full line). The numerical results take the finite corner curvature h_0 = 0.6 mm and initial profile half-width w_0 = 0.8 mm into account. The errorbars account for deviations from a perfect power-law fit from the data in (a).

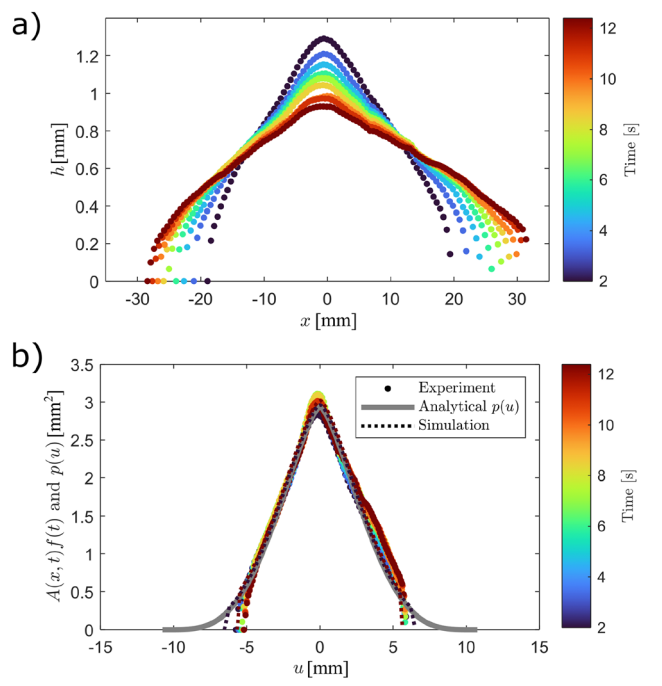

Fig. 3 (a) Droplet profiles for an experiment with XG concentration of 2 g L^{-1} for 9 different times in the range t = 2.0–12.4 s shown in the colorbar. (b) The dots show the experimental values of $A(x, t)\, f(t)$. The analytical result for the function $p(u)$ of eqn (17) using the value n = 0.48 is plotted as a gray line, while the simulations that take the finite corner curvature h_0 = 0.6 mm and initial profile half-width w_0 = 0.8 mm, are shown for the initial and final times. The diffusion constant resulting from the data fit is D_0 = 200 $mm^{1/n}$ s^{-1}.

This journal is © The Royal Society of Chemistry 2025

Open Access Article. Published on 07 ervence 2025. Downloaded on 04.02.2026 12:14:37.
This article is licensed under a Creative Commons Attribution 3.0 Unported Licence.

curvature radius h_0 along the corner of the wedge is used so that the normalization $\int \mathrm{d}x A(x, t) = V_0$ is verified. This is achieved by subtracting from the approximately triangular cross section of the ideal wedge a smaller triangular area that represents the empty region beneath the curved segment, see Fig. 1d. This correction is further described in the ESI.†

Having shown that the spontaneous spreading of a droplet of a power-law fluid in a wedge is governed by a non-linear diffusion equation, we have proceeded *via* an analytic solution of this equation to obtain the rheological exponents of several power-law fluids by simple experimental measurements. In classical (Fickian) diffusion, the position of the diffusing front grows in time as $x \propto t^{1/2}$. In our system, by contrast, the exponent differs from 1/2, a hallmark of anomalous diffusion. Specifically, the spreading follows $x_{\mathrm{tip}} \propto t^{\tau}$, where τ was typically found to be smaller than 0.3 for the shear-thinning fluids tested (sub-diffusive behavior). The connection between the anomalous diffusion exponent τ and the fluid rheology exponent n is expressed in eqn (14), a key result of our work and the theoretical basis for our experiments.

In our corner geometry the τ-exponent depends sufficiently strongly on the rheological exponent n so as to make it experimentally possible to determine n from τ. The measured τ-values are in the range $\sim$0.16–0.42. By contrast, comparable experiments[38] that study xanthan gum fluids spreading on a flat surface obtain τ values that are limited to the range $\sim$0.05–0.1. These values are too small, or too limited in range to allow for the determination of n. From a physical perspective this difference in sensitivity is likely linked to the difference in the nature of the driving forces between the two geometries: in a wedge of small opening angle the capillary pressure, which drives the flow, is negative and increases as $1/h$ as the film thins down towards the tip. On a flat surface ($\alpha = \pi$), on the other hand, the driving mechanism is the moving contact line where the capillary pressure is set by some dynamic contact angle without a similar $1/h$-increase. In a sharp corner the contact line motion is primarily normal to the flow direction, at least when $|\partial h/\partial x| \ll 1$, while it is along the flow direction on a flat plane. In our theoretical description we have taken the capillary pressure to be governed by the curvature in the transverse direction, ignoring the smaller contribution due to the curvature in the flow direction. At the critical value $\alpha = \pi - 2\Theta$, the fluid surface has no curvature in the direction transverse to the flow. As α is increased past this critical value the capillary pressure due to this curvature changes sign. This signals the transition to a different flow regime, where the capillary pressure of the sharp corner geometry is replaced by a weaker pressure. In the case of spreading on a flat substrate, the pressure is entirely controlled by the curvature in the flow direction.

Carrying out the experiments for a range of different liquids, we have observed robust behavior in the sense that experimental artifacts like inertial effects, gravity, corner curvature, pinning effects, variability in the contact angle, and finally the crossover to Newtonian behavior at small shear rates, do not dominate in the end the measurements of the rheological exponent.

Conflicts of interest

There are no conflicts to declare.

Data availability

Data for this article including experimental videos for the different power-law fluids employed are available at Zenodo at **https://doi.org/10.5281/zenodo.15046745**.

Acknowledgements

We thank Alex Hansen, Per Arne Rikvold and Erika Eiser for helpful discussions during the execution of this project. This work was partly supported by the Research Council of Norway through its projects 262644 (Center of Excellence funding scheme), 324555 (Researcher Project for Young Talent) and 301138 (NANO2021 program).

Notes and references

1 E. Steudle and C. A. Peterson, *J. Exp. Bot.*, 1998, **49**, 775–788.
2 *Growth, Dissolution and Pattern Formation in Geosystems*, ed. B. Jamtveit and P. Meakin, Kluwer, Dordrecht, 1999.
3 M. Tuller, D. Or and L. M. Dudley, *Water Resour. Res.*, 1999, **35**, 1949–1964.
4 P. Meakin and A. M. Tartakovsky, *Rev. Geophys.*, 2009, **47**, RG3002.
5 P. Concus and R. Finn, *Proc. Natl. Acad. Sci. U. S. A.*, 1969, **63**, 292–299.
6 A. Carlson, G. Bellani and G. Amberg, *Phys. Rev. E*, 2012, **85**, 045302.
7 P. G. de Gennes, *Rev. Mod. Phys.*, 1985, **57**, 827–863.
8 J. Van Hulle and N. Vandewalle, *Soft Matter*, 2023, **19**, 4669–4675.
9 J. H. Snoeijer and B. Andreotti, *Annu. Rev. Fluid Mech.*, 2013, **45**, 269–292.
10 F. Irgens, *Rheology and Non-Newtonian Fluids*, Springer International Publishing, Cham, Switzerland, 2016.
11 E. Bingham, *An Investigation of the Laws of Plastic Flow*, U.S. Government Printing Office, 1917.
12 P. Coussot, *J. Fluid Mech.*, 1999, **380**, 363–376.
13 W. R. Schowalter, *Mechanics of non-Newtonian fluids*, Pergamon Press, London, England, 1978.
14 D. R. Heldman, D. B. Lund and C. M. Sabliov, *Handbook of food engineering*, CRC Press, Boca Raton, FL, 3rd edn, 2019.
15 T. Benezech and J. F. Maingonnat, *J. Food Eng.*, 1994, **21**, 447–472.
16 P. Bertsch, L. Savorani and P. Fischer, *ACS Omega*, 2019, **4**, 1103–1109.
17 G. Phillips and P. Williams, *Handbook of Hydrocolloids*, Elsevier Science, 2009.
18 A. Deblais, E. d Hollander, C. Boucon, A. E. Blok, B. Veltkamp, P. Voudouris, P. Versluis, H.-J. Kim, M. Mellema, M. Stieger, D. Bonn and K. P. Velikov, *Nat. Commun.*, 2021, **12**, 6328.
19 J.-P. Bouchaud and A. Georges, *Elsevier Phys. Rep.*, 1990, **195**, 127–293.

Open Access Article. Published on 07 ervence 2025. Downloaded on 04.02.2026 12:14:37.
This article is licensed under a Creative Commons Attribution 3.0 Unported Licence.

20 E. G. Flekkøy, A. Hansen and B. Baldelli, *Front. Phys.*, 2021, **9**, 41.
21 A. Hansen, B.-S. Skagerstam and G. Tørå, *Phys. Rev. E*, 2011, **83**, 056314.
22 S. Gorthi, S. Meher, G. Biswas and P. Mondal, *Proc. R. Soc. A*, 2020, **476**, 20200496.
23 R. Pattle, *Mechanics Appl. Math.*, 1959, **12**, 407–409.
24 M. Tuller and D. Or, *Water Resour. Res.*, 2001, **37**, 1257–1276.
25 F. Hoogland, P. Lehmann, R. Mokso and D. Or, *Water Resour. Res.*, 2016, **52**, 8413–8436.
26 M. Moura, E. G. Flekkøy, K. J. Måløy, G. Schäfer and R. Toussaint, *Phys. Rev. Fluids*, 2019, **4**, 094102.
27 P. Reis, M. Moura, G. Linga, P. A. Rikvold, R. Toussaint, E. G. Flekkøy and K. J. Måløy, *Adv. Water Resour.*, 2023, **182**, 104580.
28 J. G. Savins, *Ind. Eng. Chem.*, 1969, **61**, 18–47.
29 W. J. Cannella, C. Huh and R. S. Seright, SPE Annual Technical Conference and Exhibition, 1988.
30 T. Sochi and M. J. Blunt, *J. Pet. Sci. Eng.*, 2008, **60**, 105–124.
31 U. Eberhard, H. J. Seybold, E. Secchi, J. Jiménez-Martnez, P. A. Rühs, A. Ofner, J. S. Andrade, Jr and M. Holzner, *Sci. Rep.*, 2020, **10**, 11733.
32 N. M. Lima, J. Avendaño and M. S. Carvalho, *J. Braz. Soc. Mech. Sci. Eng.*, 2022, **44**, 144.
33 F. Lanza, A. Rosso, L. Talon and A. Hansen, *Transport in Porous Media*, 2022, **145**, 245–269.
34 S. An, M. Sahimi, T. Shende, M. Babaei and V. Niasar, *Phys. Fluids*, 2022, **34**, 023105.
35 H. Fyhn, S. Sinha and A. Hansen, *Front. Phys.*, 2023, **11**, 1175426.
36 L. Zhang, Z. Yang, Y. Méheust, I. Neuweiler, R. Hu and Y. Chen, *Water Resources Res.*, 2023, **59**, e2023WR034958.
37 V. Starov, A. Tyatyushkin, M. Velarde and S. Zhdanov, *J. Colloid. Interface Sci.*, 2003, **257**, 284–290.
38 S. Rafai and D. Bonn, *Physica A*, 2005, **358**, 58–67.
39 A. Ponomarenko, D. Queré and C. Clanet, *J. Fluid Mech.*, 2011, **666**, 146–154.
40 R. Wijnhorst, T. C. de Goede, D. Bonn and N. Shahidzadeh, *Langmuir*, 2020, **36**, 13784–13792.
41 *Rheology of Complex Fluids*, ed. A. P. Deshpande, J. M. Krishnan and P. B. S. Kumar, Springer, New York, 2010.
42 P. J. Carreau, *Transact. Soc. Rheol.*, 1972, **16**, 99–127.
43 S. Ansari, M. A. I. Rashid, P. R. Waghmare and D. S. Nobes, *SN Appl. Sci.*, 2020, **2**, 1787.
44 S. Jouenne and B. Levache, *J. Rheol.*, 2020, **64**, 1295–1313.
45 E. Guyon, J. P. Hulin, L. Petit and C. D. Mitescu, *Physical Hydrodynamics*, Oxford University Press, London, England, 2nd edn, 2014.
46 R. L. Hoffman, *J. Colloid Interface Sci.*, 1975, **50**, 228.
47 P. Sheng and M. Zhou, *Phys. Rev. A*, 1992, **45**, 5694.
48 M. Latva-Kokko and D. H. Rothman, *Phys. Rev. Lett.*, 2007, **98**, 254503.
49 S. H. Tan, N.-T. Nguyen, Y. C. Chua and T. G. Kang, *Biomicrofluidics*, 2010, **4**, 32204.
50 P. J. Whitcomb and C. W. Macosko, *in Rheology of Xanthan Gum Solutions*, American Chemical Society, 1977, pp. 160–173.

 This journal is © The Royal Society of Chemistry 2025